ICAS-88-5.9.1

AERODYNAMIC APPLICATIONS OF AN EFFICIENT INCOMPRESSIBLE NAVIER-STOKES SOLVER

Peter-M. Hartwich and C.-H. Hsu
Vigyan Research Associates, Inc.
Hampton, Virginia

James M. Luckring and C. H. Liu
NASA Langley Research Center
Hampton, Virginia

ABSTRACT

A robust and accurate upwind scheme based on flux-difference splitting for three-dimensional, incompressible flows in general coordinates is described. Viscous effects are included through a thin-layer approximation to the Navier-Stokes equations. Turbulent flows are simulated with extensions to the Baldwin-Lomax turbulence model. Central differencing of the viscous shear fluxes and a total variation diminishing (TVD)-like discretization of the inviscid fluxes yield second-order spatial accuracy. Fairly rapid convergence to steady-state solutions is achieved with a hybrid technique which combines approximate factorization (AF) with relaxation. The effects of accuracy and gridding on the computed flow field results are assessed. The results obtained from the code for vortical flows over a delta wing, a double delta wing, and a tangent-ogive forebody compare well with experimental data.

I. INTRODUCTION

Following conventional wisdom (cf. refs. 1-3 and 4-6), before a production version of a numerical code is worth pursuing, it has to prove its mettle in various stages: (i) algorithm development, (ii) numerical experiments on accuracy, stability, and convergence, and (iii), perhaps most important, code validation using well-documented experiments and/or calculations. After having extensively and almost completely documented the first two stages [7-9] including some show case calculations [10,11], here we will concentrate on the validation phase of an implicit high resolution upwind scheme by Hartwich and Hsu [7] for the three-dimensional, incompressible Navier-Stokes equations in their thin-layer approximation.

This paper is structured as follows: first, we will briefly review the salient numerical ingredients of the numerical scheme. We will highlight the major enhancement to that scheme, that is the implementation of the algebraic turbulence model by Baldwin and Lomax [12], and its extensions to accommodate flows with massive separation. After some comments on gridding and boundary conditions, we will discuss numerical flow field results for vortical flows around a thin (t/c=0.021), slender (AR=1) sharp edged delta wing [13], around a thin (t/c=0.006) round edged double delta wing (AR=2.05) [14], and over a 3.5 caliber tangent-ogive forebody [15-17].

II. DIFFERENTIAL EQUATIONS

The governing equations are the Navier-Stokes equations in their thin-layer approximation for three-dimensional, incompressible flow. They are written in generalized curvilinear coordinates

$$\partial_t(Q/J) + \partial_\zeta E + \partial_\xi F + \partial_\eta(G-G_v) = 0 \qquad (2.1)$$

with

$$Q = (p,u,v,w)^T$$

$$E = (\beta U,\ uU+\zeta_x p,\ vU+\zeta_y p,\ wU+\zeta_z p)^T$$

$$F = (\beta V,\ uV+\xi_x p,\ vV+\xi_y p,\ wV+\xi_z p)^T$$

$$G = (\beta W,\ uW+\eta_x p,\ vW+\eta_y p,\ wW+\eta_z p)^T$$

$$G_v = (Re \cdot J)^{-1} \begin{pmatrix} 0 \\ \psi_1 u_\eta + \psi_2 \eta_x \\ \psi_1 v_\eta + \psi_2 \eta_y \\ \psi_1 w_\eta + \psi_2 \eta_z \end{pmatrix}$$

where

$$\psi_1 = \eta_x^2 + \eta_y^2 + \eta_z^2 \qquad \psi_2 = (\eta_x u_\eta + \eta_y v_\eta + \eta_z w_\eta)/3$$

$$U = \zeta_x u + \zeta_y v + \zeta_z w \qquad V = \xi_x u + \xi_y v + \xi_z w$$

$$W = \eta_x u + \eta_y v + \eta_z w$$

$$J^{-1} = x_\zeta(y_\xi z_\eta - y_\eta z_\xi) + x_\xi(y_\eta z_\zeta - y_\zeta z_\eta) + x_\eta(y_\zeta z_\xi - y_\xi z_\zeta)$$

$$\zeta_x = (y_\xi z_\eta - y_\eta z_\xi) \qquad \zeta_y = -(x_\xi z_\eta - x_\eta z_\xi)$$

$$\zeta_z = (x_\xi y_\eta - x_\eta y_\xi) \qquad \xi_x = (y_\eta z_\zeta - y_\zeta z_\eta)$$

$$\xi_y = -(x_\eta z_\zeta - x_\zeta z_\eta) \qquad \xi_z = (x_\eta y_\zeta - x_\zeta y_\eta)$$

$$\eta_x = (y_\zeta z_\xi - y_\xi z_\zeta) \qquad \eta_y = -(x_\zeta z_\xi - x_\xi z_\zeta)$$

$$\eta_z = (x_\zeta y_\xi - x_\xi y_\zeta).$$

The parameter β gives a measure for the amount of artificial compressibility, which couples the equation of continuity with the equations of motion. That, in turn, allows to integrate (2.1) like a conventional set of time-parabolic set of partial differential equations. Equation (2.1)

recovers the governing equations for truly incompressible flow for large β or in the asymptotic limit $p_t \to 0$ for $t \to \infty$. We will present only steady state solutions of (2.1), for which $\beta=1$ turned out to be quite a good choice [7,8].

The equations are nondimensionalized, where the Cartesian coordinates are scaled by some reference length, the Cartesian velocities by the free stream velocity V_∞, and the pressure is written as $C_p/2$. All terms in (2.1) are divided by the constant density ρ, and the dimensionless time is non-dimensionalized with V_∞ and the reference length. The effective Reynolds number is defined by

$$Re^{-1} = Re^{-1}_{lam} + Re^{-1}_{turb} \tag{2.2}$$

The "turbulent" Reynolds number, Re_{turb}, comprises the eddy viscosity μ_t, which is computed from the two-layer, algebraic turbulence model by Baldwin and Lomax [12]. Using their model with a non-dimensional notation yields

$$Re^{-1}_{turb} = \begin{cases} (Re^{-1}_{turb})_{inner}, & y \leq y_{crossover} \\ (Re^{-1}_{turb})_{outer}, & y > y_{crossover} \end{cases} \tag{2.3}$$

where y is the local distance normal to the body surface and $y_{crossover}$ is the smallest value of y for which $(Re^{-1}_{turb})_{inner} = (Re^{-1}_{turb})_{outer}$. In the inner region

$$(Re^{-1}_{turb})_{inner} = \ell^2 |\omega| \tag{2.4}$$

where

$$\ell = k y \{1-\exp[-(y^+/A^+)]\} \tag{2.5}$$

with

$$|\omega| = [(u_y-v_x)^2+(v_z-w_y)^2+(w_x-u_z)^2]^{1/2} \tag{2.6}$$

and the law-of-the-wall coordinate

$$y^+ = y(Re_{lam} \cdot \partial u/\partial y|_{wall})^{1/2} \tag{2.7}$$

For attached boundary-layer flows, the "turbulent" Reynolds number in the outer region is defined as

$$(Re_{turb})^{-1}_{outer} = K\, C_{cp} F_{wake} F_{Kleb} \tag{2.8}$$

K and C_{cp} are constants, and F_{Kleb} is the Klebanoff intermittency factor, and

$$F_{wake} = \min(CWK \cdot (\Delta\tilde{V})^2 \cdot y_{max}/F_{max};\ y_{max} F_{max}) \tag{2.9}$$

where

$$\Delta\tilde{V} = (u^2+v^2+w^2)^{1/2}_{max} - (u^2+v^2+w^2)^{1/2}_{min}$$

and F_{max} is the maximum of the function

$$F(y) = |\omega| \ell / k$$

with $y_{max} = y(F_{max})$. The constants are given in Ref. 12.

III. METHOD

The derivation of the up to third-order accurate high resolution schemes and an evaluation of their coupling with various implicit algorithms are found in Refs. 7 and 8. Here, we shall dwell only on areas which are pertinent to our applications.

A. Implicit Algorithm

The implicit finite-difference algorithm applied to Eq. (2.1) results in an hybrid scheme where a symmetric planar Gauss-Seidel relaxation is used in ζ-direction and approximate factorization in ξ- and η-direction.

$$[M-B^-_{j+1/2}\Delta_{j+1/2} + B^+_{j-1/2}\Delta_{j-1/2}]^n [M^{-1}]^n$$
$$[M-(C^-+Z)_{k+1/2}\Delta_{k+1/2} + (C^++Z)_{k-1/2}\Delta_{k-1/2}]^n \Delta Q^n$$
$$= -RES(Q^n, Q^{n+1}) \tag{3.1}$$

where

$$M = (I/\tau J) + A^-_{i+1/2} + A^+_{i-1/2}, \quad (I: \text{identity matrix})$$

and

$$\Delta Q^n = Q^{n+1} - Q^n, \qquad \Delta_{j-1/2}() = ()_j - ()_{j-1}.$$

The residual $RES(Q^n, Q^{n+1})$ comprises the difference approximations to the spatial derivatives in (2.1), and it is nonlinearly updated while sweeping back and forth in ζ-direction. The steady-state solutions are independent of the time step size τ due to the delta form of (3.1). Each of the one-dimensional implicit factors requires a block tridiagonal inversion in each crossplane. This algorithm gives the best of both worlds: it is unconditionally stable for linear systems like a line-relaxation method, and it is vectorizable like a three-dimensional AF scheme.

The Jacobians $A^\pm$, $B^\pm$, $C^\pm$ stem from the coefficient matrices A, B, and C, which are obtained from $(\partial E/\partial Q)$, $(\partial F/\partial Q)$, and $(\partial G/\partial Q)$, respectively, and they are written as

$$A,B,\text{ or } C = \begin{pmatrix} 0 & a\beta & b\beta & c\beta \\ a & au+\theta & bu & cu \\ b & av & bv+\theta & cv \\ c & aw & bw & cw+\theta \end{pmatrix} \qquad (3.2)$$

where $\theta=au+bv+cw$, and, for example, to obtain A, $a=\zeta_x$, $b=\zeta_y$, $c=\zeta_z$. It is easily shown [7,8,18,19] that (3.2) has a complete set of real eigenvalues

$$\Lambda = \text{diag}(\lambda_1,\lambda_2,\lambda_3,\lambda_4) = \text{diag}(\theta-S,\theta+S,\theta,\theta) \qquad (3.3)$$

(diag: diagonal matrix)

where $S=[\theta^2 + \beta(a^2+b^2+c^2)]^{1/2}$. Consequently, the matrices A, B, and C can be split according to the sign of their eigenvalues, for instance

$$A^-_{i+1/2} = (R\Lambda^- L)_{i+1/2} \quad \text{and} \quad A^+_{i-1/2} = (R\Lambda^+ L)_{i-1/2} \qquad (3.4)$$

with $\Lambda^\pm = (|\Lambda|\pm\Lambda)/2$.

The columns of R and the rows of L are the linearly independent right and left eigenvectors, respectively, and for simplicity, they are defined to give an orthonormal set, that is RL=I. An implicit algorithm always benefits from such a splitting since it allows to use one-sided differences which augments the diagonal dominance of the coefficient matrices in (3.1). Various splitting concepts [20,21] can be employed to accomplish the splitting sketched above for incompressible flow. We have been advocating the flux difference splitting concept by Roe [21] for reasons which will become apparent in the next section.

The implicit formulation is (3.2) contains also a Jacobian, Z, which stems from the viscous shear flux G_v. Applying Steger's [1] arguments, Z is derived as

$$Z = (\text{Re}\cdot J)^{-1}\begin{pmatrix} 0 & 0 & 0 & 0 \\ 0 & z_{22} & z_{32} & z_{42} \\ 0 & z_{32} & z_{33} & z_{43} \\ 0 & z_{42} & z_{43} & z_{44} \end{pmatrix} \qquad (3.5)$$

with

$$z_{22} = 4\eta_x^2/3 + \eta_y^2 + \eta_z^2 \qquad z_{33} = \eta_x^2 + 4\eta_y^2/3 + \eta_z^2$$
$$z_{32} = \eta_x\eta_y/3 \qquad z_{43} = \eta_y\eta_z/3$$
$$z_{42} = \eta_x\eta_z/3 \qquad z_{44} = \eta_x^2 + \eta_y^2 + 4\eta_z^2/3$$

B. Spatial Differences

We discuss first the differencing of the viscous shear fluxes. Using second-order central differencing, the second term in G_v, for example, reads

$$(\text{Re}\cdot J)^{-1}_{k\pm 1/2}\left(\psi_{1,k\pm 1/2}\,\Delta_{k\pm 1/2}\,u + \psi_{2,k\pm 1/2}\,\eta_{x,k\pm 1/2}\right)$$

with

$$\psi_{2,k\pm 1/2} = (\eta_{x,k\pm 1/2}\,\Delta_{k\pm 1/2}\,u + \eta_{y,k\pm 1/2}\,\Delta_{k\pm 1/2}\,v + \eta_{z,k\pm 1/2}\,\Delta_{k\pm 1/2}\,w)/3.$$

The metric quantities at the half points are computed from arithmetic averages of the values at the neighboring full points, where they are calculated using a special averaging procedure [7,8] to maintain free stream.

The flux difference splitting (FDS) is based on Roe's [21] approximate Riemann solver which computes approximate solutions to a Riemann problem by finding exact solutions to an approximate problem

$$\partial_t Q + \partial_x H = \partial_t Q + D(Q_L,Q_R)\partial_x Q = 0 \qquad (3.6)$$

where the subscripts R and L indicate the right and left states of a Riemann problem. Although (3.6) looks like a nonconservative formulation, it can be made conservative just by using appropriate averages $D(Q_L,Q_R)$ for compressible [21] and incompressible flow [7,8]. This is an important feature recalling that

$$D\partial_x Q = \partial_x(DQ) = \partial_x H$$

does not apply to incompressile flow, since its fluxes are not homogeneous of degree one in Q [20]. Furthermore, Roe's FDS accounts for all different waves by which neighboring states of a Riemann problem interact, which gives it an edge in accuracy over competing splitting concepts [22].

We found these features of FDS attractive enough to employ it in the discretization of the inviscid fluxes. Although not the optimum [7,8,23,24], the FDS is adapted to multi-dimensional problems by applying it independently in each coordinate direction and then summing up over all spatial differences. Up to third-order accurate upwinding is achieved by using TVD-like discretization techniques [7]. Here, we use only second-order accurate upwind differences for three reasons: (i) they are simpler and computationally slightly less expensive, (ii) the overall accuracy of the scheme is of at most second order due to the differencing of the viscous shear fluxes, and (iii) test calculations confirmed that results obtained with the second-order and the third-order upwinding differ only marginally [7].

The backward difference formula to obtain, for instance, $(E^n_{i-1/2})^+$, is

$$(E^n_{i-1/2})^+ = R^n_{i-1/2}\{\Lambda^+_{i-1/2}[I+0.5(\Phi^-_i-\Phi^+_{i-1})]\}^n \cdot \Delta_{i-1/2} W^n \quad (3.7a)$$

with the change in the characteristic variables given by

$$\Delta_{i-1/2} W^n = L^n_{i-1/2}\,\Delta_{i-1/2} Q^n$$

The corresponding forward difference formula for $(E^n_{i+1/2})^-$ reads

$$(E^n_{i+1/2})^- = R^n_{i+1/2}\{\Lambda^-_{i+1/2}[I-0.5(\Phi^-_{i+1}-\Phi^+_i)]\}^n \cdot \Delta_{i+1/2} W^n \quad (3.7b)$$

where $\Phi^\pm_i = \mathrm{diag}(\phi^\pm_1,\phi^\pm_2,\phi^\pm_2,\phi^\pm_4)_i$ are modified min mod limiters [7]

$$\phi^\pm_{m,i} = \max(0,\ \min(1, r^\pm_{m,i}, 2r^\mp_{m,i\pm1})) \quad (3.8)$$

with

$$r^\pm_{m,i} = \begin{cases} (\Delta_{i-1/2} w^n_m/\Delta_{i+1/2} w^n_m)^{\pm1} & \text{for } \Delta_{i\pm1/2} w^n_m \neq 0 \\ 0 & \text{for } \Delta_{i\pm1/2} w^n_m = 0 \end{cases} \quad (3.9)$$

C. Implementation of the Turbulence Model

Since the conventional turbulence model by Baldwin and Lomax [12] is too dissipative for flow calculations with massive separations [25], we modified this algebraic turbulence model in the spirit of Degani and Schiff [25].

For the delta wing calculations, we monitor the solution in each crossplane by marching from the upper and lower half of the symmetry plane toward the leading edge. Along each radial line j (lower surface) and jmax+1-j (upper surface), we compute F(y) and take its first maximum off the body surface to make sure that F_{max} is truly associated with the boundary layer flow and not with its too large value in the core of the primary or secondary vortex. That relative extremum of F(y) is detected when $F(y)<0.9F_{max}$ for $y>y_{max}$. To assure spanwise continuity in the eddy viscosity, we specify a cutoff distance $y_{cutoff,j}$ with $y_{cutoff,j}=1.5y_{max,j-1}$ along the lower surface; an analogous formula is employed along the upper surface. Transition is modeled in an ad-hoc fashion.

For the body of revolution computations, we employ a different strategy: we invoke the Degani-Schiff turbulence model only in regions of massive crossflow separation. To this end, the solution is monitored in each crossplane by marching from the windward toward the leeside meridian along a circumferential grid line a few step sizes off the body surface. The onset of massive crossflow separation is detected by the first occurrence of a negative product of two consecutive crossflow velocities. Let that location be defined by $(i,j)_{ms}$. For $i<i_{ms}$ and/or $j<j_{ms}$, the flow is assumed to be either laminar or turbulent; in the latter case the Baldwin-Lomax model is turned on. The transition from laminar to turbulent attached flow is estimated using the Esch factor which approximates the effects of angle of attack on the streamline length [26].

D. Implementation of Boundary and Initial Conditions

The boundaries are treated explicitly. This leads to a flexible scheme where subroutines setting the boundary conditions can be plugged in or pulled out of a code to (i) account for the various mesh types (e.g., C-O-, or O-O-type grids), and (ii) to avoid major changes in the implicit algorithms. We abandoned implicit implementations of the boundary conditions because of their complexity and since they failed to significantly improve the convergence performance. Except for one implicit algorithm [27], which we have dropped in the meantime, all variants of our scheme showed little to no sensitivity to the implementation of the boundary conditions.

At the far field boundaries free stream values are specified, except along the outflow boundary where a first-order extrapolation in combination with p=const=0 is used. Along the symmetry plane, reflection conditions are specified. On the body surface u=v=w=0, and the pressure is computed from a limiting form of the Navier-Stokes equations taken at a solid surface

$$p_y = Re^{-1} v_{yy} \quad (3.10)$$

with v and y assumed to be normal to the surface. Equation (3.10) is evaluated using second-order accurate finite-difference approximations. In case there is a wake cut, averaging across the wake ensures continuity. The limiters $\Phi^\pm_\ell$ (ℓ=i,j or k) are set to zero along all boundaries, leading to a first-order error at the boundaries. The intermediate boundary conditions during the implicit solution are set to zero. The initial procedure is to use uniform free stream flow with u=v=w=0 along the body surface.

IV. RESULTS

Solutions are shown for a sharp-edged delta wing, for a round-edged double delta wing, and for a tangent-ogive forebody at various Reynolds numbers and angles of attack. The CPU time per grid point and per iteration is about 35 (70) microseconds on a CYBER 205 vector computer with four (two) pipelines using 32-bit word arithmetic; it is about 90 microseconds on a Cray 2 computer in single processor mode using 64-bit word arithmetic. Reasonable results which show the basic features of the vortical flow around the aforementioned geometries are obtained on grids with 100K to 250K grid points after 300 to 500 iterations, which translates to computing times ranging from 20 minutes to three hours.

A. Flows About a Delta Wing

The wing geometry is taken from Hummel's [13] wind tunnel model. The flow field is discretized using an H-C grid (H in chordwise, C in spanwise direction). Three crossplane grids are generated at the apex, at the first station downstream of the apex, and at the trailing edge as solutions to elliptic systems [28]. All other crossplane grids are generated from extrapolation and interpolation. The cross-sectional grids are adapted to the actual wing thickness distribution through shearing. The crossplanes are clustered in the apex and in the trailing edge region, whereas they are spaced with $\Delta x/c=0.1$ for $0.3<x/c<0.7$. The circumferential spacing of the radial lines is of minor importance as long as it does not introduce too strong a curvature of the radial lines, for instance, close to the leading edge. A geometric progression is used for the radial stretching with the ratio between the minimum and maximum step size being restricted not to exceed the common bound [2,7,8,29,30] of about three orders of magnitude.

Figure 1 shows a comparison between a computational and an experimental surface oil flow pattern [13] which are very similar to each other. The angle of attack is 20.5 degrees, and Re=0.9 million. The flow separates along the sharp leading edges and rolls up into the primary vortex. The induced flow reattaches close to the centerline and is directed outboard, forming a secondary separation at about 2/3 of the local semispan. The flow induced by the secondary vortex reattaches very close to the leading edge where it partly merges with the shear layer forming the primary vortex, and partly it is directed inboard, separating for a third time.

Figure 2 illustrates some grid effects on the computed flow field results for $\alpha=20.5$ degrees and Re=0.9 million. Computed (lines) spanwise surface pressure distributions are compared with experimental data [13] (symbols) at x/c=0.3, 0.5, 0.7, and 0.9. The computations are carried out on grids with 49×49×37, 65×65×37, and 97×97×37 grid points in radial, circumferential, and longitudinal direction, respectively. The number of crossplanes has been varied between 37 and 78 without noticing any discernable differences in the cp-distributions for a given number of grid points per crossplane. The integration domain has the shape of a half cylinder with radius $R_{max}/c=2$ and it extends from one root chord upstream of the apex to one root chord aft of the trailing edge; the grid extent is of minor importance (see below). We consider the results calculated on the 97×97×37 grid as spatially converged as indicated by a comparison with computations on a 65×97×37 (cf. Fig. 3) and a 97×129×37 grid (not shown here).

The necessity to account for transition which was observed in the experiment [13] is demonstrated in Fig. 3. The flow is assumed to be fully laminar along the lower wing surface and for $x/c<0.6$ along the upper surface. The effect of turbulence is clearly seen for $x/c>0.7$: the fully laminar calculation (Fig. 2c) considerably overpredicts the strength of the secondary vortex while the transitional computation is in much closer agreement with the experiment [13].

The representative convergence history in Fig. 4 highlights two issues: (i) converged results are obtained after 300 to 500 iterations, and (ii) cross-sectional grids with 65×65 grid points already suffice to obtain a basically converged asymptotic lift.

The predicted lift agrees quite well with experimental data over a wide α range (Fig. 5). The computed loads with the turbulence model being invoked differ only marginally from those in Fig. 5. The delta wing produces negative lift at $\alpha=0$ degrees because of its negative camber. Maximum lift occurs between 30 and 35 degrees in both experiment and computation. This peak is associated with the onset of vortex breakdown at the trailing edge. For $\alpha=40$ degrees, the vortex burst occurs at $0.4<x/c<0.45$ in good agreement with similar experiments [31,32] (Fig. 6). As in experiments [33], we observe a smooth transition from the confined flow along the primary vortex core upstream of the vortex breakdown into the bubble-shaped region of reversed flow.

B. Flows Over a Double Delta Wing

Vortical flows are computed around a round-edged double delta wing [14] with an aspect ratio of 2.05 and a maximum thickness of t/c=0.006. The leading edges of the strake and of the wing have an 80 and 60 degree sweep, respectively, with a leading-edge kink at x/c=0.5. The integration domain is discretized by using grids of H-C topology with 53 to 81 crossplanes perpendicular to the longitudinal wing axis. Shape and extent of the integration domain are similar to the one used in the delta wing calculations. The cross-sectional grids are again generated as solutions to elliptic systems [28] with the same constraints as for the delta wing. Figure 7 shows a comparison between a computed (line) and a measured (symbols) spanwise surface pressure distribution for x/c=0.75, $\alpha=12$ degrees, and Re=1.3 million. This calculation was done on a grid with 53 crossplanes, each consisting of 97 by 167 grid points in radial and circumferential direction, respectively. Even when using such fine cross-sectional grids, the computed pressure "footprints" of the strake and the wing vortex indicate that either even finer grids are needed or that the accuracy of the scheme needs to be enhanced, to match not only the location but also the suction of the experimentally observed vortices. Nevertheless, it is already possible to trace the interaction of the strake and wing vortices over the entire wing as indicated by the total pressure contours for various root-chord stations in Fig. 8.

Figure 9 shows the convergence histories for computations on a 65×101×81 grid with α = 12, 20, and 40 degrees, and Re=1.3 million. The more complex double delta wing calculations require between 50 and 100 percent more iterations than the delta wing computations.

The measured variation of lift with angle of attack [14] is compared with an calculation by Fujii and Schiff [34] and with present results in Fig. 10. Up to maximum lift at about $\alpha=25$ degrees, both computational results match the experimental values quite closely. Beyond $C_{L,max}$, only the present calculations compare well with the experiment. Again, $C_{L,max}$ is associated with the onset of vortex breakdown at the trailing

edge. A flow field result with a simulated vortex breakdown is depicted by means of particle traces in Fig. 11 for α=40 degrees. As before, this result suggests that a vortex breakdown is not an abrupt event but that it is more of a smooth, gradual nature.

C. Flows Over a Tangent-Ogive Forebody

C-O-type meshes are used to compute vortical flows around a 3.5 caliber tangent ogive, mounted on a circular cylinder [15,16,17]. The radial grid lines are equiangularly spaced with the same radial stretching as used for the delta wing calculations. Figure 12 shows the effect of the integration domain extent and of cross-sectional resolution on normal force. The baseline gird in Fig. 12(a) consists of 65x73x40 grid points corresponding to R_{max}/d=28. Retaining the same grid density, the computational domains of lesser extent are obtained by dropping radial points in the far field (i.e., R_{max}/d=13.22 corresponds to a 58x73x40 grid, etc.). We recognize a second-order accurate convergence of the normal force when correlated with the representative step size $h=(imax \cdot jmax)^{-1/2}$, where imax and jmax give the number of grid points in vertical and circumferential direction. We consider this quasi two-dimensional apporoach in the grid refinement study justified since the number of crossplanes has been varied from 40 to 105 without detecting any discernable changes in the loads or in flow details like the surface pressure distribution. The length of the circular cylinder has been changed between 7 and 35 base diameters. For the afterbody exceeding x/d=20, we encountered difficulties in converging our solutions to a stable steady state. We identified two sources for this problem: (i) unsteady vortex shedding along the afterbody, and (ii) an insufficient resolution of these body vortices due to the longitudinal stretching of the grid. The effects of gridding on the convergence performance and on the normal force development is illustrated in Fig. 13 for the four cases shown in Fig. 12.

Figure 14 shows comparisons of measured and computed surface pressure coefficients for four axial stations: x/d=0.5, 2.0, 3.5, and 6.0 diameters downstream of the body apex. Three different calculations are shown for Re=0.2 million and α=20 degrees. First, the computations with our modifications to the turbulence model are shown by the solid line. Second, a completely laminar computation is shown for comparison by the dashed line, and third, a more sophisticated, but still conventional approach is employed by using the Degani-Schiff modification of the Baldwin-Lomax turbulence model. For x/d<3.5, the flow is apparently laminar, and all calculations match the experimental pressure data quite closely. The turbulence models are invoked for x/d>3.0. For x/d>3.5, the laminar calculation clearly overpredicts the influence of the primary vortex in the pressure distribution and locates its position at too low an azimuthal angle. The third approach still gives too strong a primary vortex at too low an azimuthal angle, and it fails to capture the laminar separation bubble in the equatorial regime. With our modified turbulence model, the position of the primary vortex is less than five degrees off, its suction is of comparable (x/d=3.5) and equal (x/d=6.0) strength, and the effect of the laminar separation bubble on the equatorial C_p-distribution can be clearly seen. Our extension to the Baldwin-Lomax turbulence model works also successfully for other flow conditions as indicated by the results for Re=0.8 million and α=30 degrees in Fig. 15.

CONCLUDING REMARKS

A numerical method to solve three-dimensional, incompressible viscous flow problems have been demonstrated for complex vortical flows over simple aerodynamic shapes. Such flow field studies are interesting in their own right, as they show the current major hurdle in routinely predicting such flows: the lack of dependable turbulence and transition models. Since it is relatively fast and proved to be quite accurate in several instances, the present scheme appears to be a viable choice for a research code to work these problems. When being more oriented towards production code development, a multiblock capability needs to be incorporated to handle complex geometries.

Acknowledgment

NASA Langley Research Center sponsored the work of the first two authors under NASA Contract No. NAS1-17919.

REFERENCES

[1] Steger, J.L., "Implicit Finite-Difference Simulation of Flow About Arbitrary Two-Dimensional Geometries," AIAA Journal, Vol. 16, No. 7, July 1978, pp. 679-686.

[2] Pulliam, T.H. and Steger, J.L., "Implicit Finite-Difference Simulations of Three-Dimensional Compressible Flow," AIAA Journal, Vol. 18, No. 2, Feb. 1980, pp. 159-167.

[3] Pulliam, T.H. and Steger, J.L., "Recent Improvements in Efficiency, Accuracy, and Convergence for Implicit Approximate Factorization Algorithms," AIAA Paper 85-0360, Jan. 1985.

[4] Anderson, W.K, Thomas, J.L., and Van Leer, B., "A Comparison of Finite-Volume Flux Vector Splittings for the Euler Equations," AIAA Journal, Vol. 24, No. 9, Sept. 1986, pp. 1453-1460.

[5] Thomas, J.L. and Walters, R.W., "Upwind Relaxation Algorithms for the Navier-Stokes Equations, AIAA Journal, Vol. 25, No. 4, April 1987, pp. 527-534.

[6] Thomas, J.L., Taylor, S.L., and Anderson, W.K., "Navier-Stokes Computations of Vortical Flows over Low Aspect Ratio Wings," AIAA Paper 87-0207, Jan. 1987.

[7] Hartwich, P.-M. and Hsu, C.-H., "High Resolution Upwind Schemes for the Three-Dimensional, Incompressible Navier-Stokes Equations," AIAA Paper 87-0547, Jan. 1987, also: AIAA Journal, Vol. 26, No. 7, July 1988.

[8] Hartwich, P.-M., Hsu, C.-H., and Liu, C.H., "Vectorizable Implicit Algorithms for the Flux-Difference Split, Three-Dimensional Navier-Stokes Equations, "Symposium on

Parallel Processor Applications in Fluid Mechanics, 1987 ASME Fluids Engineering Conference, Cincinnati, Ohio, June 1987, also to appear in ASME Journal of Fluids Engineering.

[9] Hartwich, P.-M., Hsu, C.-H., and Liu, C. H., "Total Variation Diminishing (TVD) Schemes of Uniform Accuracy," NASA TM 100552, Jan. 1988.

[10] Hsu, C.-H., Hartwich, P.-M., and Liu, C. H., "Computation of Vortical Interaction for a Sharp-Edged Double Delta Wing," Journal of Aircraft, Vol. 25, No. 3, March 1988.

[11] Hsu, C.-H., Hartwich, P.-M., and Liu, C. H., "Incompressible Navier-Stokes Computations for a Round-Edged Double Delta Wing," Journal of Aircraft, Vol. 25, No. 7, July 1988.

[12] Baldwin, B.S. and Lomax, H., "Thin-Layer Approximation and Algebraic Turbulence Model for Separated Turbulent Flows," AIAA Paper 78-257, Jan. 1978.

[13] Hummel, D., "On the Vortex Formation Over a Slender Delta Wing at Large Angles of Attack," AGARD-CP-247, Paper No. 15, April 1978.

[14] Brennenstuhl, U. and Hummel, D., "Vortex Formation over Double-Delta Wings," ICAS-82-6.6.3, August 1982.

[15] Lamont, P.J., "The Effect of Reynolds Number on Normal and Side Forces on Ogive Cylinders at High Incidence," AIAA Paper 85-1799, August 1985.

[16] Keener, E.R., "Flow-Separation Patterns on Symmetric Forebodies," NASA TM 86016, Jan. 1986.

[17] Hall, R.M., private communication.

[18] Steger, J.L. and Kutler, P., "Implicit Finite-Difference Procedures for the Computation of Vortex Wakes," AIAA Journal, Vol. 15, No. 4, April 1977, pp. 581-590.

[19] Rizzi, A. and Eriksson, L. E., "Computation of Inviscid Incompressible Flow with Rotation," Journal of Fluid Mechanics, Vol. 153, April 1985, pp. 275-312.

[20] Steger, J.L. and Warming, R.F., "Flux Vector Splitting of the Inviscid Gasdynamics Equations with Application to Finite-Difference Methods," Journal of Computational Physics, Vol. 40, No. 2, April 1981, pp. 263-293.

[21] Roe, P.L., "Approximate Riemann Solvers, Parameter Vectors, and Difference Schemes," Journal of Computational Physics, Vol. 43, No. 2, October 1981, pp. 357-372.

[22] Van Leer, B., Thomas, J.L., Roe, P.L., and Newsome, R.W., "A Comparison of Numerical Flux Formulas for the Euler and Navier-Stokes Equations," AIAA Paper 88-1104-CP, June 1987.

[23] Roe, P.L., "Characteristic Based Schemes for the Euler Equations," Annual Review of Fluid Mechanics, Vol. 18, 1986, pp. 337-365.

[24] Davis, S.F., "A Rotationally Biased Upwind Difference Scheme for the Euler Equations," Journal of Computational Physics, Vol. 56, No. 1, October 1984, pp. 65-92.

[25] Degani, D. and Schiff, L.B., "Computation of Turbulent Supersonic Flows Around Pointed Bodies Having Crossflow Separation," Journal of Computational Physics, Vol. 66, No. 1, September 1986, pp. 173-196.

[26] Polhamus, E. C., "A Review of Some Reynolds Number Effects Related to Bodies at High Angles of Attack," NASA CR 3809, August 1984.

[27] Hartwich, P.-M., Hsu, C.-H., and Liu, C. H., "Implicit Hybrid Schemes for the Flux Difference Split, Three-Dimensional Navier-Stokes Equations," Lecture Notes in Physics, Vol. 264, Springer-Verlag, New York, 1986, pp. 303-307.

[28] Hartwich, P.-M., "Three-Dimensional Grids as Solutions of Elliptic Systems," AIAA Paper 86-0430, January 1986.

[29] Rumsey, C.L., Thomas, J.L., Warren, G.P., and Liu, G.C., "Upwind Navier-Stokes Solutions for Separated Periodic Flows," AIAA Journal, Vol. 25, April 1987, No. 4, pp. 535-541.

[30] Blottner, F.G., "Variable Grid Scheme Applied to Turbulent Boundary Layers," Computer Methods in Applied Mechanics and Engineering, Vol. 4, 1974, pp. 179-194.

[31] Payne, F.M., Ng, T.T., Nelson, R.C., and Schiff, L.B., "Visualization and Flow Surveys of the Leading Edge Vortex Structure on Delta Wing Planforms," AIAA Paper 86-0330, January 1986.

[32] Wentz, Jr., W. H. and Kohlman, D. L., "Vortex Breakdown on Slender Sharp-Edged Wings," Journal of Aircraft, Vol. 8, No. 3, March 1971, pp. 156-161.

[33] Roos, F. W., private communication.

[34] Fujii, K. and Schiff, L.B., "Numerical Simulation of Vortical Flows over a Strake-Delta Wing," AIAA Paper 87-1229, June 1987.

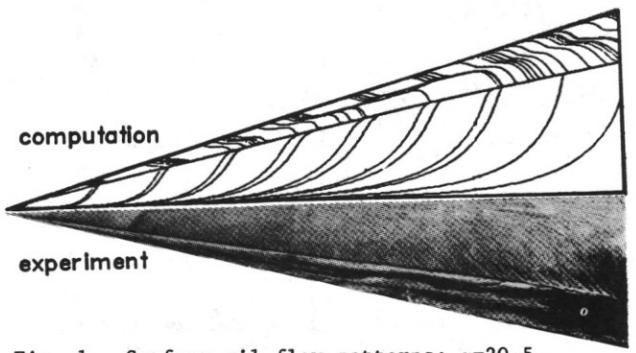

Fig. 1. Surface oil flow patterns; α=20.5, Re=0.9 million.

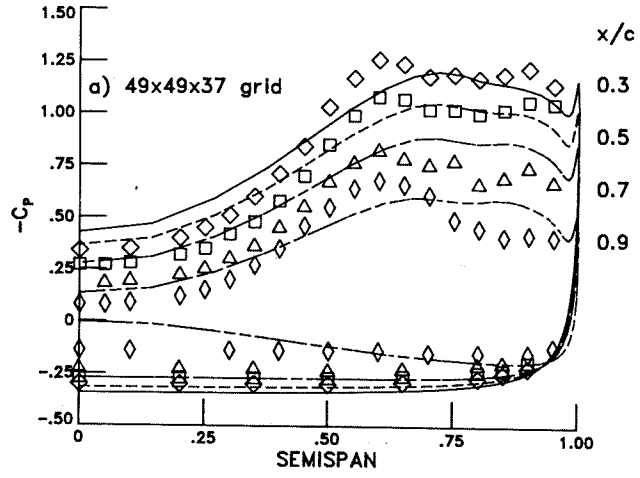

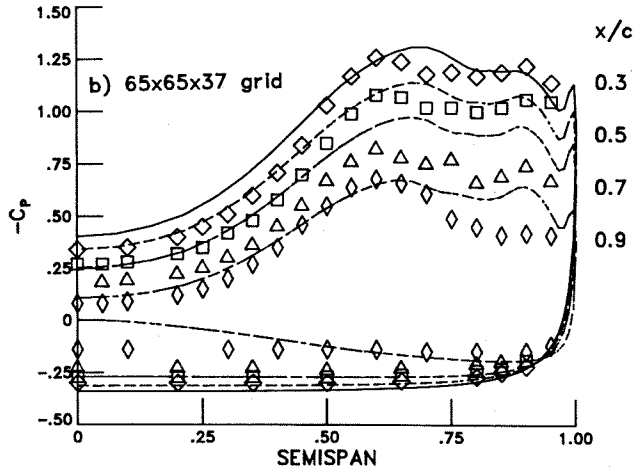

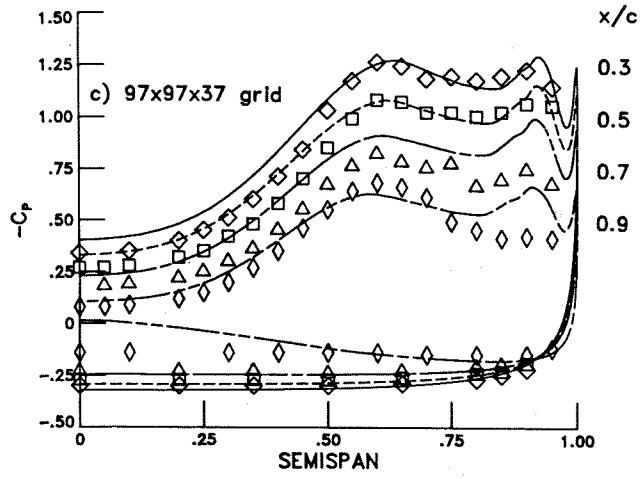

Fig. 2. Experimental (symbols) and computational (lines) spanwise surface pressure distributions - computations for laminar flow; 20.5 degrees, Re=0.9 million.

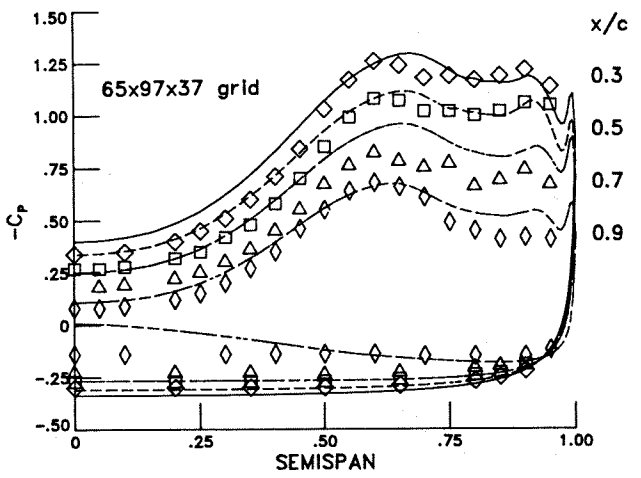

Fig. 3. Experimental (symbols) and computational (lines) spanwise surface pressure distributions - computation for transitional flow; α=20.5 degrees, Re=0.9 million.

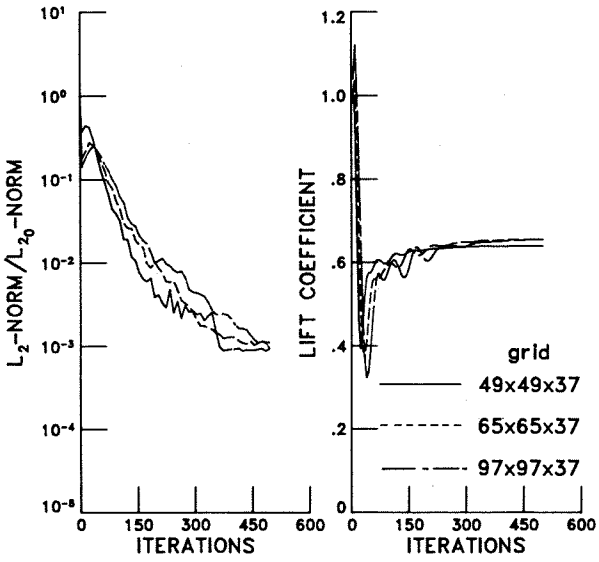

Fig. 4. Convergence summary for delta wing calculations; α=20.5 degrees, Re=0.9 million (laminar).

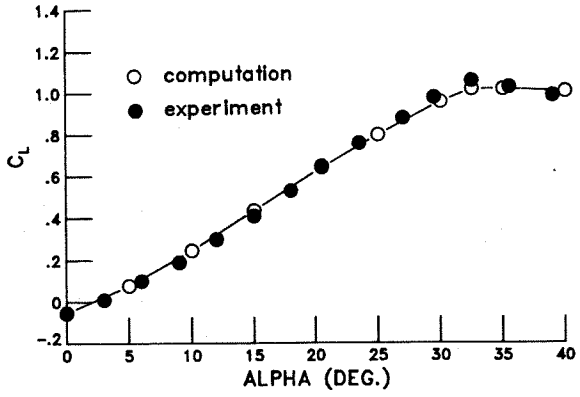

Fig. 5. Variation of lift with angle of attack for a delta wing; Re=0.9 million.

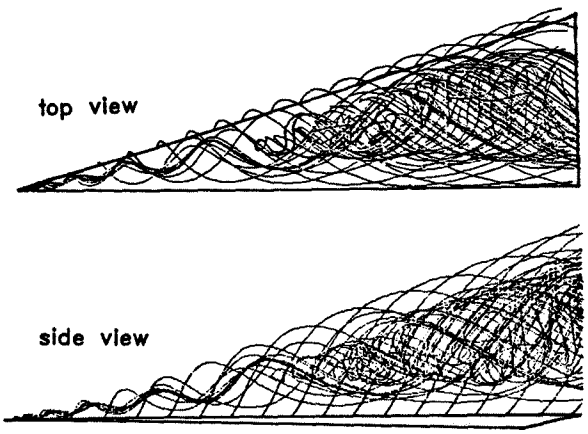

Fig. 6. Flow over a delta wing with a vortex burst (particle traces); α=40 degrees, Re=0.9 million (laminar).

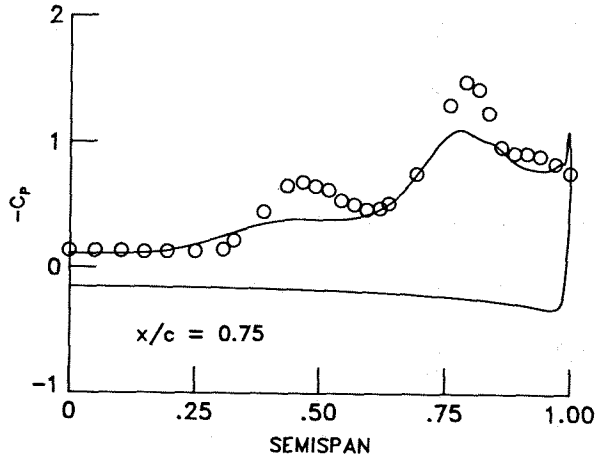

Fig. 7. Experimental (symbols) and computational (line) spanwise surface pressure distributions - computation for laminar flow; α=12 degrees, Re=1.3 million.

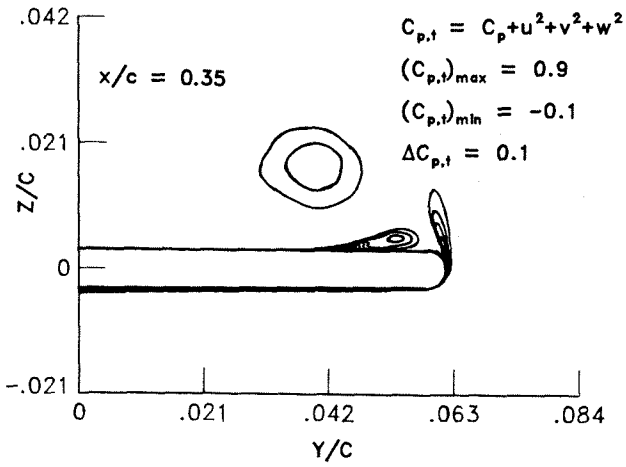

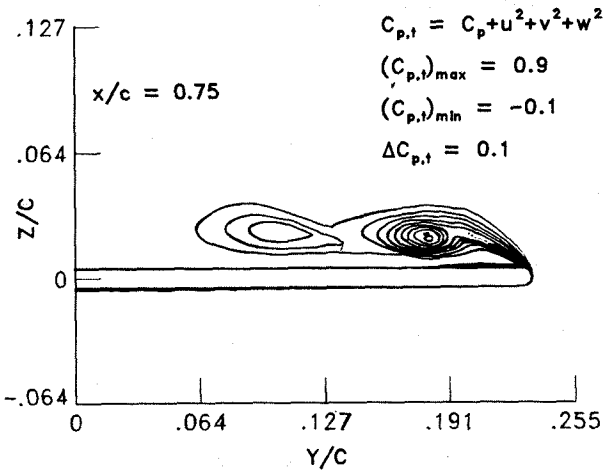

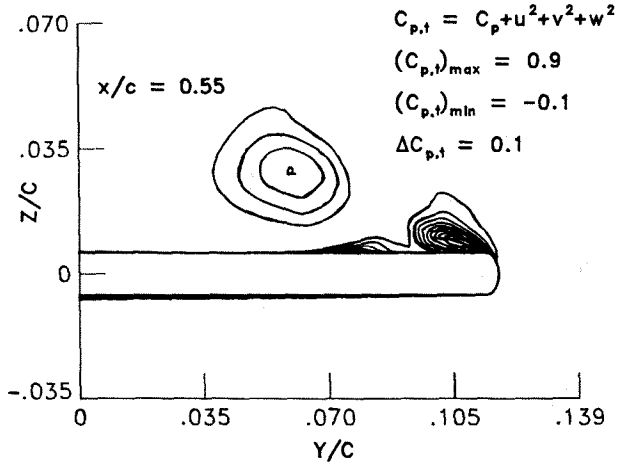

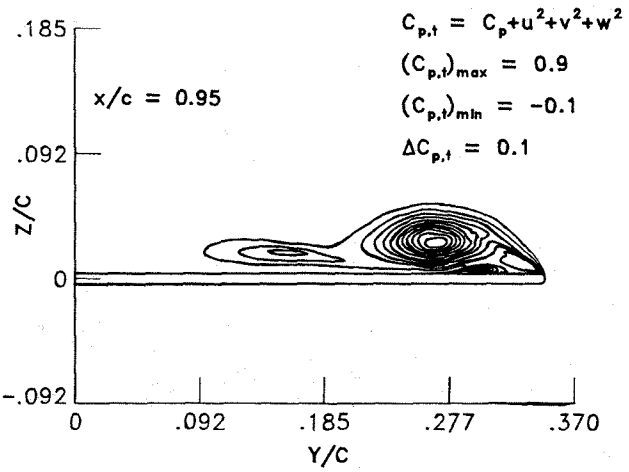

Fig. 8. Cross-section total pressure distributions for a double delta wing; α=12 degrees, Re=1.3 million (laminar).

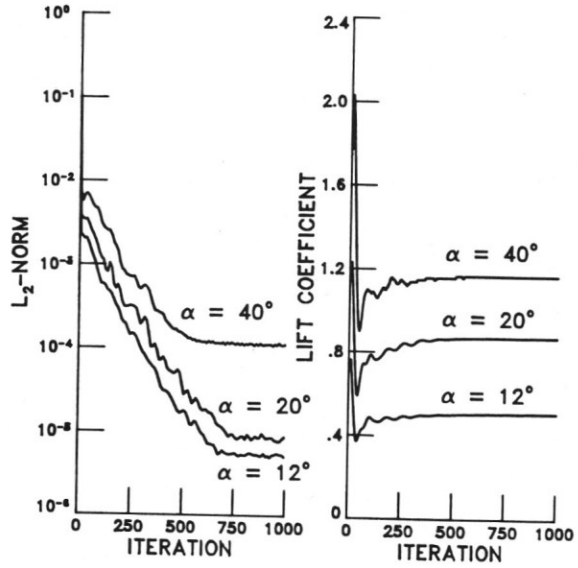

Fig. 9. Convergence summary for double delta wing calculations; 65×101×81 grid, Re=1.3 million (laminar).

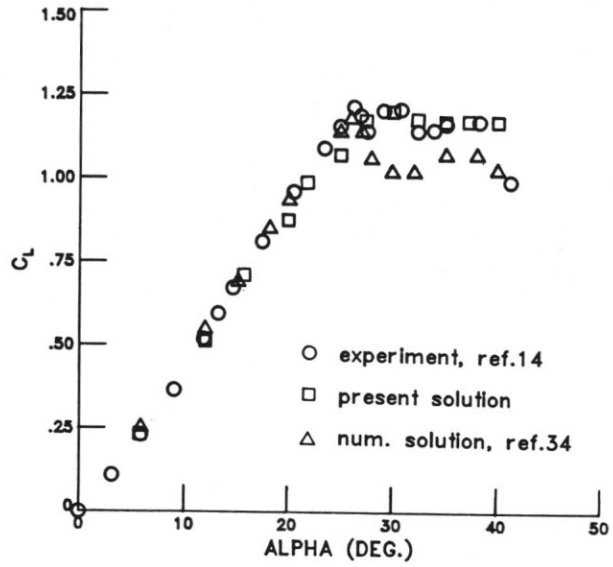

Fig. 10. Variation of lift with angle of attack for a double delta wing; Re=1.3 million.

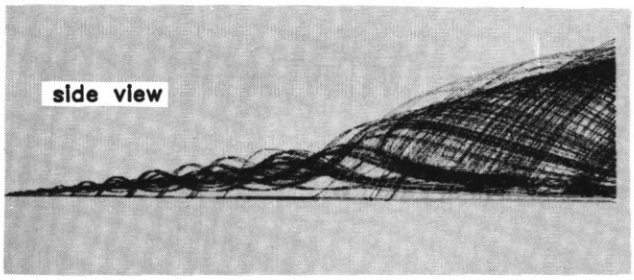

Fig. 11. Flow over a double delta wing with a vortex burst; α=40 degrees, Re=1.3 million (laminar).

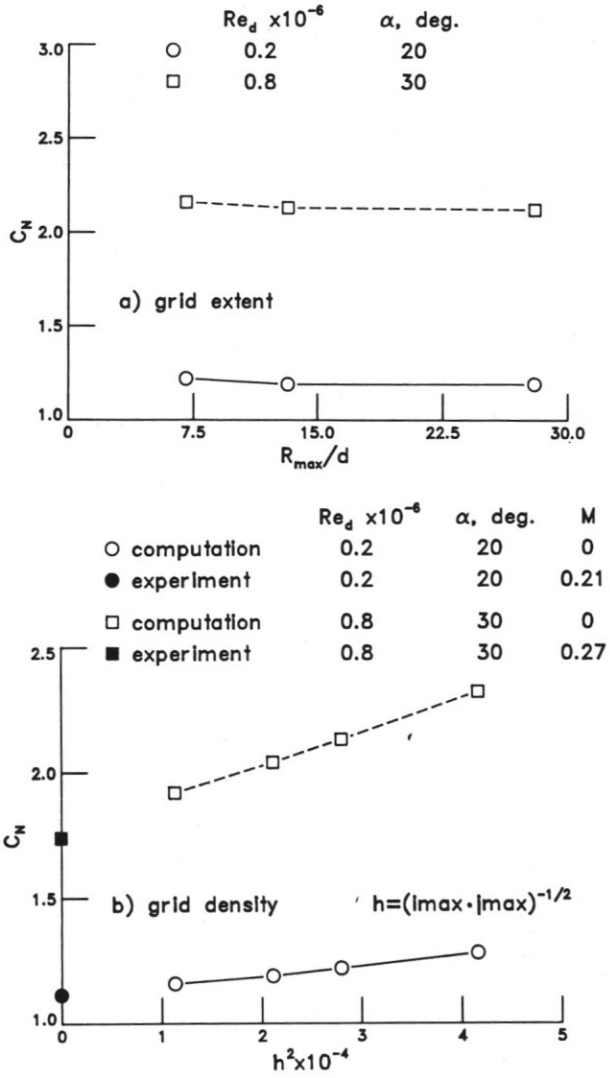

Fig. 12. Grid effects on computed normal force for a tangent ogive forebody.

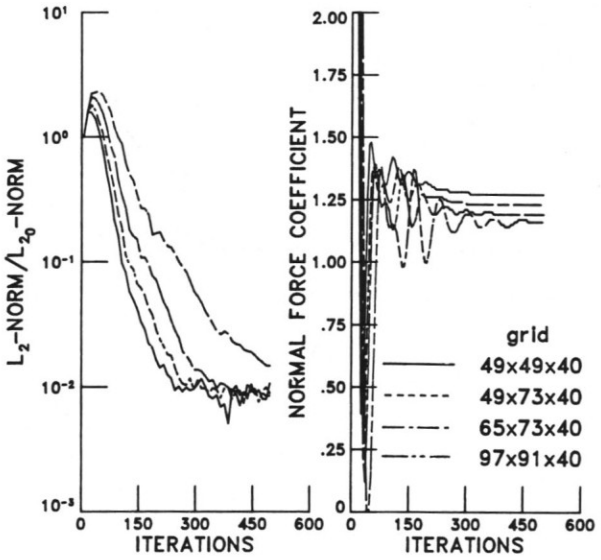

Fig. 13. Convergence summary for tangent ogive calculations; α=20 degrees, Re=0.2 million (transitional).

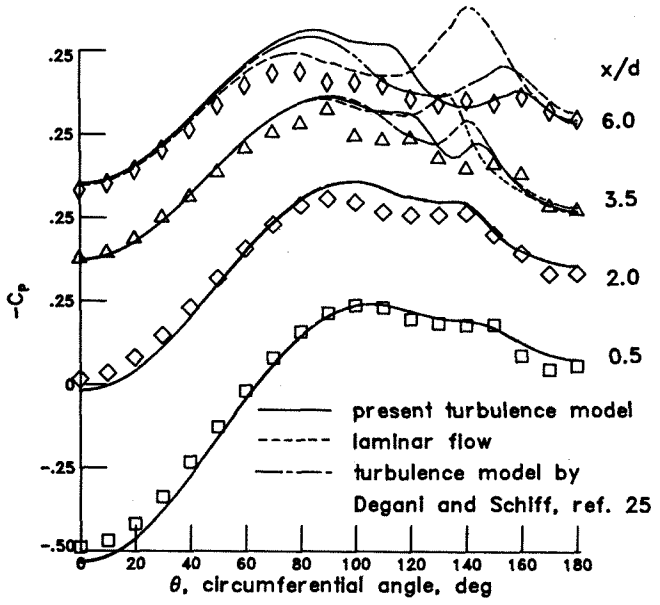

Fig. 14. Experimental (symbols) and computational (lines) circumferential surface pressure distributions; α=20 degrees, Re=0.2 million.

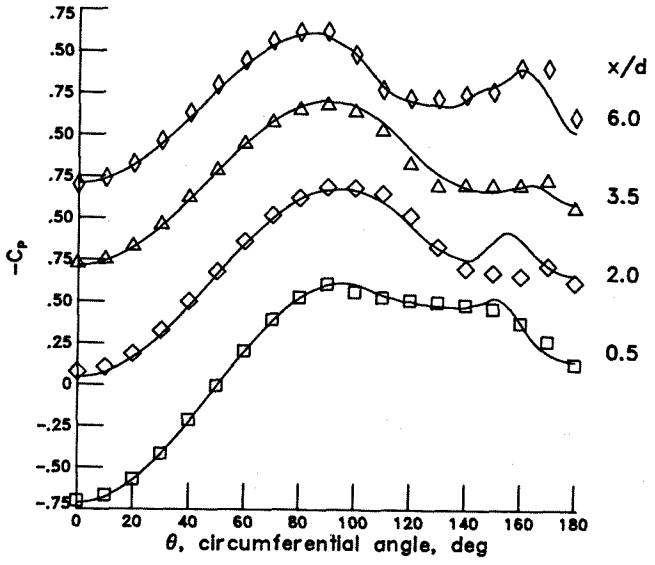

Fig. 15. Experimental (symbols) and computational (lines) circumferential surface pressure distributions; α=30 degrees, Re=0.8 million.